

# Heat Transfer and Film Cooling on a Contoured Blade Endwall with Platform Gap Leakage

**Stephen P. Lynch**

Mechanical and Nuclear Engineering Department  
The Pennsylvania State University  
University Park, PA 16802, USA  
splynch@psu.edu

**Karen A. Thole**

Mechanical and Nuclear Engineering Department  
The Pennsylvania State University  
University Park, PA 16802, USA  
kthole@psu.edu

## ABSTRACT

*Turbine blade components in an engine are typically designed with gaps between parts due to manufacturing, assembly, and operational considerations. Coolant is provided to these gaps to limit the ingestion of hot combustion gases. The interaction of the gaps, their leakage flows, and the complex vortical flow at the endwall of a turbine blade can significantly impact endwall heat transfer coefficients and the effectiveness of the leakage flow in providing localized cooling. In particular, a platform gap through the passage, representing the mating interface between adjacent blades in a wheel, has been shown to have a significant effect. Other important turbine blade features present in the engine environment are non-axisymmetric contouring of the endwall, and an upstream rim seal with a gaspath cavity, which can reduce and increase endwall vortical flow, respectively. To understand the platform gap leakage effect in this environment, measurements of endwall heat transfer and film cooling effectiveness were performed in a scaled blade cascade with a non-axisymmetric contour in the passage. A rim seal with a cavity, representing the overlap interface between a stator and rotor, was included upstream of the blades and a nominal purge flowrate of 0.75% of the mainstream was supplied to the rim seal. Results indicated that endwall heat transfer coefficients increased as platform gap net leakage increased from 0% to 0.6% of the mainstream flowrate, but net heat flux to the endwall was reduced due to high cooling effectiveness of the leakage flow.*

## INTRODUCTION

Gaps between turbine components are present in an engine due to assembly constraints of stationary-rotating component clearances. High-pressure cool air from the compressor is provided to the gaps to minimize hot gas ingestion into regions that are uncooled under the airfoil platforms. In addition to preventing ingestion, the high pressure coolant flow can be used to improve cooling of the components on the hot gas path side, but the effect of complex vortical flow present near the leakage paths is difficult to predict, even for idealized endwalls without gaps.

A gap in the rotor endwall, referred to as a platform gap in this paper, is present between airfoils that are assembled individually on the wheel of a high-pressure turbine blade section. The platform gap between components is a necessary consequence of the manufacturing and assembly process, but also helps to accommodate thermal expansion over the wide range of turbine operating conditions. Leakage from this gap is largely directed toward the aft portion of the blade passage, since the gaspath static pressure is lowest there, and its interaction with the high-speed gaspath fluid generates high turbulence and mixing.

Another important gap is the stationary-rotating clearance gap between the stator and rotor, referred to as a rim seal in this paper. The stator-rotor endwalls around this gap are often designed to create a backward-facing step, where recirculating fluid downstream of the step helps to limit hot gas ingestion. The recirculating fluid is convected into the blade passage and can strengthen the vortical endwall flow.

Non-axisymmetric (three-dimensional) contouring of the endwall is another important recent feature of blade endwalls. The shape of the contour is designed to reduce the cross-

passage pressure gradient and weaken the vortical secondary flows. This is beneficial for the aerodynamic performance of the turbine, but also has been shown to reduce heat transfer coefficients and improve film cooling coverage relative to flat endwalls. However, contouring is rarely studied in combination with leakage flows in the literature.

For the work presented here, a realistic blade endwall was studied in a scaled-up cascade. The endwall included non-axisymmetric contouring in the passage. A rim seal, with representative leakage mass flow rates and tangential velocity of the leakage flow relative to the blade row, was included upstream of the blade. A platform gap through the passage was modeled and the effect of leakage flowrates were evaluated.

#### RELEVANT PAST STUDIES

A range of studies have been presented in the literature concerning the effect of turbine component interface gaps, all of which indicate measurable impact on the main gas path. A gap located upstream of an airfoil, such as between a combustor and a vane, or between a rotor and stator, presents a discontinuity in the endwall that impacts the development of the vortical flow generated at the endwall-airfoil junction. Abo El Ella, et al. [1] indicated a significant difference in turbine secondary flow structure and increased overall loss for a cavity upstream of a transonic cascade. A backward-facing step in the endwall upstream of a blade resulted in lower total pressure loss across the cascade than a forward-facing step in the study by de la Rosa Blanco, et al. [2], due to reduced interaction of the upstream separated flow with the blade secondary flow.

Leakage through the upstream gap generally negatively impacts performance, although it can be used to improve component durability. Piggush and Simon [3] indicated an increase in

loss roughly following the increase in momentum flux ratio for leakage flow through an upstream slot simulating the combustor-vane gap. Turbine stage efficiency decreased with increasing stator-rotor leakage flowrate in the study by Reid, et al. [4]. Simulations showed an increase in entropy generation (loss generation) where the leakage flow mixed into the freestream. Thrift, et al. [5] showed a dramatic difference in the development of the horseshoe vortex upstream of a vane as a function of slot orientation angle, with a 45° slot essentially eliminating the development of the vortex and providing almost 150% improvement in coolant coverage. A series of studies (Popović and Hodson [6], Popović and Hodson [7], Popović and Hodson [8]) investigated leakage from realistic rim seals with representative tangential velocity. Their work showed the importance of a recirculating vortex in the upstream cavity on aerodynamic loss generation, with the best performance when the vortex was moved further into the rim seal and the blade-vane overlap was made as smooth as possible. The effect of tangential leakage velocity on loss was low for low purge flow rates but helped to better distribute coolant across the platform.

A platform gap between individual turbine components in a wheel also has detrimental effects on turbine performance. Reid, et al. [9] measured a 0.46% drop in turbine efficiency due to the presence of a platform gap, even with no net flow through the gap. The losses were attributed to mixing within the gap, and were shown to be relatively independent of platform gap net flowrate. Measurements in a transonic cascade by Jain, et al. [10] led them to conclude that the presence of the platform gap (without net flow) resulted in a 5% increase in overall loss, but introduction of net gap flow had negligible effect. In contrast, Piggush and Simon [3]

found a small increase in loss for increased gap flow, but loss did not change for net flowrates above 1% of the mainstream flow.

The platform gap has a dramatic impact on endwall coolant coverage. The coverage of the film cooling effectiveness was significantly reduced on a vane endwall with a platform gap, relative to a continuous endwall, in a study by Cardwell, et al. [11]. Gap flow temperatures indicated ingestion of coolant into the forward portion of the gap where it mixed with freestream fluid before being ejected near the throat. A study by Piggush and Simon [12] indicated a significant increase in vane endwall heat transfer where the platform gap leakage flow was ejected onto the endwall, compared to a smooth endwall. Lynch and Thole [13] found that ingestion and ejection of flow in the platform gap correlated well with high heat transfer coefficients on the inner channel walls of the platform gap. More recent work by Roy, et al. [14] indicated that the combined effect of an upstream purge slot and platform gap provided more coolant coverage to the endwall, although nearly all of the platform gap coolant was ejected near the trailing edge suction side platform.

As mentioned in the introduction, another feature becoming more common in turbomachines is the use of non-axisymmetric endwall contouring. Several studies have shown that the contouring reduces the cross-passage pressure gradient and weakens the development of endwall secondary flow, which is beneficial for both aerodynamic loss and endwall heat transfer. The contour studied by Gustafson, et al. [15] reduced the cross-passage pressure gradient in a cascade by up to 47%. Measurements by Knezevici, et al. [16] show how the migration of the secondary flow across the passage is delayed with contouring. The contour of Lynch, et al. [17] increased heat transfer in the forward portion of the passage, but dramatically

decreased it in a region of high heat transfer near the aft blade pressure side. Panchal, et al. [18] found that due to a shift in secondary flow due to contouring, overall heat transfer was reduced by 15% relative to a flat endwall. More recent work by Schuepbach, et al. [19], Turgut and Camci [20], and Regina, et al. [21] have investigated contouring with rim seal purge, and have generally found that contouring is still beneficial at design conditions, although performance can be worsened at off-design conditions.

Only a few studies mentioned above have considered gap-related interactions on the endwall heat transfer and film cooling for a blade endwall, such as the effect of an upstream rim cavity with tangential leakage (due to the relative motion of the rotor) and a platform gap through the passage. This study builds on the work by Popović and Hodson [6] by adding a platform gap, as well as the work of Roy, et al. [14] by including tangential flow supplied to an upstream rim cavity. Highly detailed measurements of heat transfer coefficients and film cooling effectiveness are provided to help understand the convective environment of a turbine with realistic gaps.

## EXPERIMENTAL METHODOLOGY

Heat transfer and adiabatic film cooling measurements were obtained on the endwall of a large-scale low-speed linear cascade that was matched to engine Reynolds number conditions. Flow through the cascade was provided by a closed-loop wind tunnel shown in Figure 1. Some flow was diverted into an upper bypass channel far upstream of the cascade and extracted by a blower so that it could be sent to cascade leakage features. For film cooling studies, heat exchangers in the bypass channel were connected to a 40 kW chiller unit to cool leakage air, and the mainstream was equipped with a 55 kW electric heater bank to heat

mainstream air to approximately 46°C, such that a temperature differential of approximately 25°C was achieved. The density ratio of the coolant for those studies was 1.08. For heat transfer studies, the heat exchangers were used to keep the leakage air temperature to within 0.5°C of the mainstream temperature (density ratio of 1.0).

The design and construction of the linear cascade is described in Lynch, et al. [22] and Lynch, et al. [23], and only a short description will be given here. The cascade contained six blades based on a high-pressure turbine airfoil geometry. Table 1 lists the geometric details of the cascade. Measured blade static pressures at midspan were shown to closely match the design conditions. A turbulent boundary layer was measured on the endwall upstream of the cascade and parameters are listed in Table 1. A turbulence grid located  $16C_{ax}$  upstream of the center blade of the cascade resulted in a freestream turbulence level of 6%.

Upstream of the blades, the platform (endwall) overlap geometry between the stationary vane and rotating blade rows was simulated as shown in Figure 2. The blade platform extended upstream of the blade leading edge and below the nominal endwall height, resulting in a depression referred to as a rim cavity in this study. A smooth curve was used to transition from the lowered upstream blade platform to the start of the non-axisymmetric endwall contouring in the passage. Although the cascade was designed to simulate a rotor, no part of the test section, including the upstream (stator) platform, moved relative to the blades.

Rim seal flow was simulated by a leakage feature placed upstream of the cascade. The leakage feature induced swirl to the flow, such as would occur in an engine when there is a mismatch between the rotor hub speed and the tangential velocity of the leakage flow. At a net rim seal mass flow ratio of 0.75% MFR, small turning vanes in the rim seal feature imparted a

tangential velocity component to the leakage flow relative to the blade (in the +Y direction) that was 10% of the estimated rotor hub speed, as obtained by assuming a stage degree of reaction of 0.5 (Lynch, et al. [23]). In the stationary reference frame of an engine, this would be 90% of the hub speed. Note that no part of the cascade was rotating; the effect of rotation was simulated only in the swirled leakage flow. Net mass flow through the rim seal was measured by a laminar flow element and supplied to a plenum mounted below the test section. Static pressure taps were used to check periodicity of the flow exiting the rim seal. The rim seal leakage mass flow ratio was kept constant at 0.75% MFR for all cases in this study, which resulted in a local blowing ratio of  $M=0.29$  and momentum flux ratio of  $I=0.09$ . These quantities were determined by calculating an average coolant velocity through the rim seal from the measured mass flow and rim seal metering area, as well as a local freestream velocity from measured inlet freestream total pressure and local static pressure just above the rim seal exit.

A non-axisymmetric contoured endwall, designed using the methodology described by Praisner, et al. [24], was employed in the passage of the cascade (see Figure 3). Note that the endwall contour in this study differs from typical designs in that there is a hill near the leading edge suction side, as opposed to the depression found in most other contour designs (Harvey, et al. [25], Praisner, et al. [24]). Simulations performed by MacIsaac, et al. [26] for a flat endwall with the same rim seal geometry indicate a large recirculation vortex in the rim cavity that changes the trajectory of the suction side horseshoe vortex around the airfoil leading edge, relative to a smooth endwall. As might be expected, the generation of the optimal endwall contour shape is dependent on the complicated endwall flowfield present with an upstream cavity. The contour in this study was designed for nominal rim seal leakage conditions of 0.75%

MFR. The platform gap, however, was not included in the optimization but was included in the experiment.

The effect of a gap between adjacent blade platforms was considered for all cases in this study. The geometry of the platform gap is depicted in Figure 3, and gaps were located in every passage except between blades 1 and 2, where the gap would pass below the tailboard. A thin strip seal was attached to the underside of the platform gap to simulate the effect of a similar component in the engine which limits leakage flow into and out of the gap. Platform gap leakage flow was isolated from the rim seal leakage flow to enable independent control. Net leakage mass flow was supplied to individual plenums located under the test section. Total mass flow supplied to all four gap plenums was measured with a laminar flow element, and valves were used to split the flow evenly among the four plenums, as determined by equalizing the pressures in each of the plenums. Net gap leakage flowrates are reported in this paper as a percentage of a single blade passage mass flow rate. Net flowrates ranged from 0% to 0.6%, where the 0% net flow was achieved by closing a valve in the supply line for each gap plenum. For the 0% case, mainstream flow could still be ingested into the forward portion of the gap and ejected further downstream, but no net flow was introduced.

An estimation of the gap leakage velocities along the gap length was performed using the measured plenum pressure and net gap mass flow, similar to the method of Cardwell, et al. [11]. At a given position along the gap, a local inviscid leakage velocity ( $V_{\text{gap,inv}}$ ) was calculated using the measured platform gap plenum total pressure ( $P_{\text{tot,c}}$ ) and the local freestream static pressure ( $P_{\text{s,loc}}$ ) obtained from a 2-D simulation of the airfoil geometry:

$$V_{\text{gap,inv}} = \sqrt{\frac{2}{\rho_c} (P_{\text{tot,c}} - P_{\text{s,loc}})} \quad (1)$$

The local inviscid leakage velocities were averaged over the entire length of the gap and the average was used in the formula for net mass flow from the gap:

$$\dot{m}_{\text{gap}} = C_D \dot{m}_{\text{ideal}} = C_D (\rho_c \bar{V}_{\text{gap,inv}} A_{\text{gap}}) \quad (2)$$

where  $C_D$  is the global discharge coefficient relating the inviscid mass flow to the actual net mass flow. Since the net mass flow was measured,  $C_D$  was iterated until Eq. 2 was satisfied. Note that the global  $C_D$  for the platform does not generally conform to a standard interpretation of a discharge coefficient, since the gap can ingest and eject flow depending on the local pressure ratio across the gap. The gap velocity plotted in Figure 4 was obtained by multiplying  $V_{\text{gap,inv}}$  by the global  $C_D$ , and is normalized by the maximum gap ejection velocity for 0% net gap flow, which occurs at the farthest downstream position.

Gap leakage velocities for the three net leakage flowrates tested in this study are shown in Figure 4. For 0% gap MFR, gap leakage velocities are negative up to  $x_{\text{gap}}/L=0.42$ , implying ingestion of the mainstream gases into the gap plenum. Further along the gap, velocities are positive where the leakage flow is ejected out of the gap due to low freestream static pressure. As the net MFR is increased to 0.3%, ingestion is eliminated over the entire gap length, but the ejection velocity of the leakage flow is small, especially in the forward portion of the gap. Note that this analysis does not account for unsteady effects or for a difference between the endwall static pressure and the inviscid freestream static pressure. For the highest leakage MFR of 0.6%, ejection velocities are nearly uniform over the entire gap length and are up to twice the ejection velocity for 0% net flow.

## Heat Transfer Measurements

Infrared thermography was used to determine heat transfer coefficients by capturing spatially-resolved surface temperatures on a uniform heat flux surface (heater) attached to the endwall. Heater design and attachment to the non-axisymmetric contour was based on the methodology developed by Lynch, et al. [17]. A 3 mm thick stereolithography plate ( $k \approx 0.2$  W/m-K) was constructed in the shape of the contoured endwall shown in Figure 3a. Polyurethane foam ( $k \approx 0.032$  W/m-K) was molded to the underside of the plate to minimize conduction losses for the heat transfer experiments. The minimum foam thickness was 20 mm at the upstream edge of the blade endwall. The heater was bonded to the stereolithography plate via a vacuum-bag process. Total heater thickness, including the inconel circuit and the encapsulating kapton, was 75  $\mu\text{m}$ . A 37  $\mu\text{m}$  layer of copper was attached to the flow surface of the heater to smooth out heat flux between the circuit gaps (Kang, et al. [27]). Flat black paint was applied to the copper to increase emissivity for infrared measurements, and type-E thermocouples were thermally bonded to the underside of the heater for infrared image calibration. See Figure 1 for the locations of the thermocouples. The thermocouples were positioned so that there were at least two thermocouples per image, where one thermocouple was in a high-temperature region and the other was in a low-temperature region. Also, most of the thermocouples were visible in multiple images to improve overall calibration accuracy.

Heat flux was calculated by measuring the circuit voltage and current and dividing by the heater area, where current was measured by the voltage drop across a precision resistor in series with the heater. Conductive and radiative losses were subtracted from the total heat flux. Conductive losses were estimated locally by a one-dimensional conduction analysis to be less

than 1.5% of the total heat flux. Radiative losses were also estimated locally to be less than 15%, assuming that the surroundings behaved as a blackbody at the freestream temperature of 295 K. Local loss corrections were highest in regions of high endwall temperatures ( $\sim 315$  K).

Infrared camera images were obtained at several locations throughout the cascade to provide a complete map of the endwall heat transfer. Portholes cut into the top endwall were sequentially opened so that the IR camera could image the endwall directly without need for a window. Before capturing images in this manner, we determined through several measurements of temperature and blade static pressure that the cascade conditions were unaffected by the brief opening of the portholes. In addition, the camera was mounted in fixture that completely covered the porthole while images were being obtained. At each location, five images were captured to reduce measurement uncertainty. The averaged result was calibrated by adjusting surface emissivity and background temperature until the heater top surface temperature matched measurements from the underside-mounted thermocouples. A conduction bias, due to the heater resistance, of  $0.8^{\circ}\text{C}$  between the top surface and underside-mounted thermocouples was accounted for in the calibration. Typical emissivity and background temperature for the calibrated images was 0.96 and  $16^{\circ}\text{C}$ , respectively, which compared well to published emissivity for black paint ( $\sim 0.96$ ) and the cascade freestream temperature of  $21^{\circ}\text{C}$ . Calibrated images generally agreed to within  $0.5^{\circ}\text{C}$  of the thermocouple measurements. The camera resolution was approximately 1.4 pixels/mm at the nominal standoff distance of 0.54 m. No correction was performed for perspective distortion of the images at the upstream cavity or along the contoured endwall since the small variation in camera standoff distance did not affect its focus.

The reference temperature in the definition of the heat transfer coefficient ( $T_{in}$ ) was determined as the average of the measured freestream temperature, the rim seal plenum temperature, and the gap supply line temperature immediately upstream of the gap plenums. Variation among the averaged temperatures was kept to within 0.5°C. The ingestion mechanism of the platform gap (Cardwell, et al. [11], Lynch and Thole [13]) caused the gap plenum temperatures to be approximately 1°C higher than the reference temperature for the nominal gap leakage flowrate of 0.3% MFR, which was why gap plenum temperatures were not used in determining the reference temperature. Since the lowest endwall temperature was at least 10°C above the reference temperature, the slightly increased temperature of ejected gap flow was calculated to have a minimal effect (nearly the same order as the experimental uncertainty) on the measured heat transfer coefficient.

Uncertainty was estimated using the partial derivative method (Moffat [28]). The largest source of error was the measurement of surface temperature with the infrared camera. Bias and precision uncertainties for that parameter were 0.8°C and 0.3°C, respectively. Total uncertainty in the heat transfer coefficient, based on a 95% confidence interval, was 5% at a value of  $Nu=410$ . The uncertainty in cascade Reynolds number was 4%, dominated by the uncertainty in inlet velocity. Uncertainties in coolant flowrates were estimated at 3%.

### **Adiabatic Effectiveness Measurements**

For the film cooling effectiveness studies, a low thermal conductivity plate was used where supplemental film cooling holes ( $d/C_{ax}=0.020$ ) were drilled in the endwall around the platform gap. Figure 5 depicts the holes, with the injection directions shown by the blue arrows. Holes were grouped by their location: six holes near the pressure side of the blade platform are

designated as film cooling group #1 (FC1), two holes by the suction side trailing edge are designated as FC2, and four holes by the suction side of the blade platform are designated as FC3. Table 2 lists the L/d ratios and local surface angles of the holes.

Each group of holes had its own separate plenum for independent control, and four endwalls were constructed for film cooling tests; thus, there were four FC1 plenums, four FC2 plenums, and three FC3 plenums underneath the cascade (no film cooling was supplied on the suction side of blade 2's platform). In a manner similar to the platform gap flow supply, the total mass flow supplied to the four FC1 plenums was measured with a laminar flow element and then split evenly by equalizing the pressures in each of the FC1 plenums. The same methodology was employed for FC2 and FC3 plenum flows. The mass flow ratios and respective estimated blowing parameters (based on local freestream conditions) for each of the film cooling groups are listed in Table 2. The average coolant velocity for a given film cooling group was determined by the total mass flow divided by the sum of the hole metering areas. The average local freestream velocity for a film cooling group was estimated by using the average of the local freestream velocities at each of the hole exit locations, as determined from a 2-D CFD simulation of the cascade.

Infrared thermography was used to obtain film cooling effectiveness measurements by capturing spatially-resolved surface temperatures. A mold was used to cast polyurethane foam into the shape of the bottom endwall of the cascade (Figure 3). The flow surface of the foam was painted flat black for high emissivity, and type-E thermocouples for infrared image calibration were installed flush with the endwall surface. Calibration with the embedded endwall thermocouples yielded an average emissivity of 0.94 and an average background

temperature of 47°C (nominal inlet freestream temperature was  $T_{in}=47^{\circ}\text{C}$ ). The calibrated images were assembled into a temperature map and converted to adiabatic effectiveness using the measured freestream temperature and a coolant reference temperature.

The coolant reference temperature ( $T_c$ ) in the definition of adiabatic effectiveness was the average of the temperatures in the rim seal plenum and the film cooling plenums, as well as the temperature of the flow in the supply line leading to the platform gap plenums. Variation among the averaged coolant temperatures was less than 0.5°C. The ingestion mechanism of the platform gap resulted in gap plenum temperatures that were about 1.5°C above the supply line temperature for the nominal gap net flowrate of 0.3% MFR, which was why the gap plenum temperatures were not used to determine the reference temperature.

Uncertainty in the effectiveness measurements was estimated in the same manner as for the heat transfer measurements. The largest contribution to uncertainty was the surface temperature measured with the IR camera, which had an estimated bias uncertainty of 0.6°C and a precision uncertainty (95% confidence interval) of 0.3°C. Total uncertainty in effectiveness was  $\partial\eta=\pm 0.04$  at a value of  $\eta=0.25$ .

## RESULTS

Measurements of endwall heat transfer and film cooling effectiveness are first compared to the endwall flow pattern visualized by oil flow. The effect of the platform gap leakage flow is then discussed.

### Comparison of Oil Flow Visualization, Heat Transfer, and Film Effectiveness

Oil flow visualization was performed to obtain endwall flow patterns caused by secondary flows. The visualization was done with nominal leakage flowrates of 0.75% MFR for

the rim seal and 0.3% MFR for the platform gap. Recall that the rim seal leakage also had swirl relative to the blade, to simulate that effect in an engine. The endwalls were painted white, and a mixture of black paint, motor oil, and kerosene was uniformly applied. Images of the resulting streak pattern were captured after the pattern reached a steady-state condition (approximately two hours). Arrow-tipped streaklines were drawn over the top of the image to enhance the flow pattern, as shown in Figure 6a. Dashed lines indicate separation and attachment lines due to vortical secondary flow structures. No streaklines were drawn on the upstream platform, since a pattern was not discernable to low-velocity separated flow in the rim cavity.

Although the oil flow does exhibit some indication of classical endwall secondary flow structures, such as a passage vortex and a corner vortex, the presence of the rim cavity is dominant in the upstream patterns. A recirculation vortex is present in the cavity and is driven by the separated flow from the upstream platform. A saddle point appears to be created near the intersection of the cavity recirculation attachment and the platform gap. For the non-axisymmetric endwall contour in this study, the bulge near the suction side leading edge displaces the suction side horseshoe vortex away from the blade. It eventually turns sharply toward the blade and impinges on the blade suction side.

The effect of the platform gap is not immediately obvious in the oil flow pattern, but some observations are made. Streaklines upstream of the saddle point appear to be diverted from crossing over the gap, suggesting a small amount of leakage is emanating from the gap and blocking near-wall flow. Further downstream in the throat region, a small pool of oil and paint collects on the suction side platform near the gap. The pool appears to be located in a region between the passage vortex trajectory and the wake from the trailing edge of the blade.

Lynch and Thole [13] describe a vortical structure that is generated around this location as the gap leakage is ejected into the mainstream flow. The sweeping action of the vortical structure brings oil toward the pool.

Figure 6b shows contours of endwall heat transfer with the streaklines from Figure 6a overlaid to enable interpretation of secondary flow effects. The white line through the passage indicates the location of the platform gap. The rim cavity upstream of the blade experiences relatively low heat transfer due to the low-velocity separated flow present in that region. Flow approaching the saddle point crosses over the platform gap, which disturbs the boundary layer and increases heat transfer on the downstream side of the gap, right around the saddle point. Around the leading edge, heat transfer levels are high due to the downwash of the horseshoe vortex legs at the airfoil-endwall junction, particularly along the suction side.

Along the pressure side further into the passage, heat transfer levels are relatively low in the endwall boundary layer downstream of the horseshoe vortex. Streamwise acceleration toward the throat of the passage causes the heat transfer coefficient to increase. As the endwall boundary layer crosses over the platform gap, heat transfer rises to very high levels on the downstream side of the gap. A combination of factors contributes to the significant heat transfer increase across the gap. The endwall boundary layer is tripped by the physical presence of the gap; also, fluid travelling within the gap is ejected in the low-pressure region around the throat (see Figure 4), which results in high turbulence levels and the generation of a vortical structure described by Lynch and Thole [13]. Heat transfer downstream of the gap decreases as the thermal boundary layer re-develops, but starts to increase slightly toward the suction side trailing edge as the corner vortex grows.

Film cooling effectiveness contours are shown in Figure 6c, with the oil flow streaklines overlaid to enable correlation with secondary flow features. Areas with high effectiveness values indicate where the coolant lowers the adiabatic wall temperature and reduces the driving potential for heat transfer to the endwall. The rim seal leakage upstream of the blade provides some cooling on the platform, although the recirculating vortex in the cavity severely constrains the extent of coverage. Most of the rim seal coolant is swept to the saddle point and separates from the endwall, providing little coverage around the leading edge or the pressure side of the passage. Any rim seal leakage that might be ingested into the forward portion of the platform gap is convected along the gap and ejected near the throat, which results in a region of high effectiveness on the suction side platform. Net flow introduced into the gap plenum also preferentially leaks out in the throat region, since the endwall static pressure is lowest there. A streak of high effectiveness persists along the blade suction side in Figure 6c, which is attributed to the vortical structure mentioned earlier. Note that the four film cooling holes located on the suction side platform appear redundant in terms of providing coolant coverage; however, in the engine the flow through those holes also acts as a heat sink helping to remove heat from the platform metal.

### **Effect of Platform Gap Leakage Flow**

Contours of endwall heat transfer are shown in Figure 7 for increasing net gap flowrates. The nominal rim seal leakage flowrate of 0.75% MFR with swirl was maintained for all cases, and thus heat transfer upstream of the blades is expected to be the same. Around the location of the saddle point, heat transfer levels do not change significantly between 0% and 0.3% gap MFR, and increase slightly between 0.3% and 0.6% MFR as the gap ejection velocity increases.

Heat transfer along the pressure side of the passage in Figure 7 is unchanged by increasing gap flow since secondary flows prevent it from penetrating to that region. Around the throat on the suction side blade platform, however, heat transfer levels rise noticeably with increasing gap MFR. Increasing the amount of flow ejected results in a stronger vortical structure and increased turbulence.

Figure 8 shows endwall Nusselt numbers extracted from Figure 7 along the path of an inviscid streamline passing through the center of the passage at the inlet plane. The abscissa of the plot is the X-coordinate along the streamline normalized by the blade axial chord, such that  $X/C_{ax} = 0$  corresponds to the inlet plane of the cascade and  $X/C_{ax} = 1$  corresponds to the exit plane. The vertical bars are the regions where the streamline passes over the platform gap. For a given location along the streamline path, heat transfer values from each of the three measured blade passages were averaged to obtain a representative value for that streamwise location.

Heat transfer levels upstream of the passage are the same for the range of platform gap flowrates in Figure 8 due to similar rim seal conditions, as described earlier. Heat transfer increases along the streamline path approaching the first gap crossing ( $X/C_{ax} = -0.18$ ), due to reattachment of the recirculating rim cavity flow on the upstream endwall. Downstream of the first gap crossing, Nusselt values are higher for 0.6% gap MFR compared to the other leakage MFR's due to the larger gap ejection velocity (Figure 4). Slightly lower levels of Nu are seen in this region for 0.3% gap MFR, compared to 0% gap MFR. One possibility for this trend is that the weak ejection of gap flow at 0.3% results in lower local disturbance to the endwall thermal

boundary layer than for ingestion of gap flow (and the subsequent restart of the boundary layer) at 0% net flow.

Further along the inviscid streamline, heat transfer levels decrease along the pressure side up to  $X/C_{ax}=0.5$ , and then begin to increase again as the flow accelerates toward the throat. After the second gap crossing at  $X/C_{ax}=0.85$ , heat transfer coefficients for 0% gap MFR rise to levels nearly four times higher than the value on the upstream blade platform ( $X/C_{ax}=0.4$ ). Increasing the gap MFR to 0.6% results in a 50% increase immediately downstream of the gap relative to 0% gap MFR, and a 500% increase over the heat transfer levels on the upstream blade platform. Certainly this is undesirable for part durability due to the potential for high heat loads and large temperature gradients in the component metal. Heat transfer levels decay rapidly further along the streamline path, reaching nearly the same level regardless of gap MFR at the exit plane ( $X/C_{ax}=1$ ).

To visualize the region of influence of the gap leakage, contours of heat transfer augmentation were calculated by taking the ratio of heat transfer with the gap flowing a net positive massflow, to heat transfer with no net gap flow (0% gap). Figure 9 shows the contours of heat transfer augmentation for 0.3% and 0.6% gap MFR, where values above 1.0 indicate an increase in heat transfer relative to the 0% gap MFR case. Over the majority of the upstream half of the passage, increasing the gap MFR does not significantly increase or decrease endwall heat transfer. Along the suction side platform around the throat, however, heat transfer augmentation levels are approximately 1.3-1.4 for 0.3% gap MFR, and 1.4-1.5 for 0.6% gap MFR. The highest heat transfer augmentation generally occurs immediately downstream of the throat since leakage flow preferentially ejects from the gap at that location, but heat transfer is

augmented on the suction side blade platform along nearly the entire downstream half of the platform gap's length through the passage.

Film cooling effectiveness contours in Figure 10 give an indication of the effectiveness of gap leakage in reducing the adiabatic wall temperature. For no net gap flow (0% MFR), Figure 10a indicates that cooling due to the rim seal leakage is ingested into the forward portion of the gap, providing very little coverage over a significant portion of the endwall. As the ingested coolant is convected along the gap, its temperature increases due to mixing with the hot mainstream gases. The ingested flow is ejected out of the gap at the throat and provides some cooling to the suction side platform, although a good portion of the cooling also comes from the four film cooling holes in that region.

As the gap net MFR is increased to 0.3% (Figure 10b), the gap ejects coolant over its entire length, which is reflected in the higher effectiveness values around the gap. Cooling effectiveness is also significantly increased on the suction side platform around the throat since the net outflow limits mixing of the coolant with the hot mainstream gas before it exits onto the blade platform. Cooling effectiveness levels decay rapidly downstream of the gap due to high levels of turbulence and mixing with the mainstream. From 0.3% MFR (Figure 10b) to 0.6% MFR (Figure 10c), there does not appear to be a significant difference in cooling effectiveness for the forward portion of the passage or immediately downstream of the throat.

Figure 11 presents cooling effectiveness values along the inviscid streamline path for the three gap flow cases. Effectiveness on the upstream platform is high due to the rim seal leakage flow, but decays as the streamline progresses toward the platform gap. Immediately downstream of the first platform gap crossing ( $X/C_{ax} = -0.18$ ), the 0.3% and 0.6% gap MFR cases

indicate higher effectiveness levels than the 0% MFR case due to ejected gap flow. Cooling effectiveness decays along the streamline into the passage for all gap MFR's due to the sweeping effect of the secondary flows that prevents coolant from penetrating toward the pressure side of the platform; however, cooling persists farther along the streamline path for 0.6% gap MFR, compared to 0.3% or 0%. The spike in effectiveness at  $X/C_{ax} = 0.7$  is where the streamline crosses a film cooling hole on the pressure side platform. Downstream of the second gap crossing ( $X/C_{ax} = 0.85$ ), a net gap MFR of 0.3% causes higher effectiveness levels on the blade platform relative to 0% gap MFR, due to both increased coolant mass flow and reduced mixing within the platform gap. Increasing the gap MFR to 0.6% does not appear to significantly improve cooling effectiveness downstream of the second gap crossing relative to 0.3%, however; effectiveness levels are already high and introducing more coolant is unnecessary.

Figure 12 shows contours of net heat flux reduction (NHFR) for 0.3% and 0.6% gap MFR, where net heat flux reduction is defined as:

$$NHFR = 1 - \frac{h}{h_0}(1 - \eta\theta) \quad (3)$$

The heat transfer coefficient ratio with gap flow relative to 0% gap MFR ( $h/h_{0\%}$ ) was presented in Figure 9, and the effectiveness ( $\eta$ ) was presented in Figure 10. Note that the heat transfer coefficient measurements were performed without film cooling holes, due to the difficulty of obtaining high-quality experimental measurements around the exit of a film cooling hole. Our analysis for NHFR assumed that the heat transfer coefficient augmentation for the film cooling holes was 1.0; measurements by Sen, et al. [29] and Baldauf, et al. [30] for moderate blowing ratios indicated that heat transfer augmentation for circular film cooling holes was generally

below 1.1, so our assumption was deemed reasonable. The non-dimensional metal temperature ( $\theta$ ) was estimated to be a constant value of 1.6 per the recommendations of Sen, et al. [29]. Net heat flux reduction values less than 0 are undesirable, since they indicate where the cooling scheme results in higher heat flux to the part than the uncooled scheme. This would occur if the heat transfer coefficient augmentation increases without a significant increase in cooling effectiveness. In contrast, NHFR values greater than 0 indicate a benefit of the cooling with regards to heat flux experienced by the part.

Net heat flux reduction for 0.3% gap MFR is shown in Figure 12a. The contours are similar to the results for film cooling effectiveness (Figure 10b), especially on the upstream half of the platform, since the heat transfer augmentation is nominally equal to one there. Despite a significant increase in heat transfer augmentation on the suction side platform, the high effectiveness levels of the ejected platform gap flow result in high net heat flux reduction values and reduced heat flux to the metal, relative to the 0% gap MFR case. The contours in Figure 12b for 0.6% gap MFR closely resemble the results for 0.3% gap MFR, indicating that an increase in heat transfer coefficients due to higher gap MFR is offset by increased cooling.

The overall effect of increasing gap leakage flow was determined by performing an area-weighted average of the endwall heat transfer and film cooling effectiveness results over the entire platform. Figure 13 shows the percent increase in area-averaged Nusselt number and area-averaged film effectiveness for the two net gap flowrates, relative to 0% gap MFR. Also included in the figure is the area-weighted average NHFR. The inset in the figure indicates the averaging area. Platform averages for each of the three platforms were then averaged to get an overall result. At the nominal gap MFR of 0.3%, area-averaged endwall heat transfer increased

by 6% but film effectiveness increased by 17% relative to 0% gap MFR, suggesting that the additional cooling massflow could reduce the overall heat load on the part. In fact, the area-averaged NHFR in Figure 13 was 0.33, indicating a reduction in heat flux to the endwall for the nominal gap MFR case.

For the higher gap MFR of 0.6%, the endwall Nusselt number increased by 8% but overall cooling increased by 27%, relative to the 0% gap MFR case. Most of the additional cooling benefit for 0.6% gap MFR versus 0.3% gap MFR is probably due to higher effectiveness around the upstream portion of the platform gap (see Figure 10). The average NHFR for 0.6% gap MFR was 0.35, which is only slightly higher than for 0.3% gap MFR. For a turbine designer desiring to conserve coolant massflow without sacrificing part durability, there appears to be no significant benefit in increasing the platform gap net massflow above 0.3%.

## CONCLUSIONS

Endwall heat transfer and film cooling effectiveness measurements were presented for a turbine blade with a realistic contoured platform geometry that included an upstream rim seal cavity and a platform gap between adjacent blade endwalls. Leakage flows at representative engine mass flow rates were provided at the upstream rim seal and through the platform gap.

Oil flow visualization revealed the features of secondary flow influenced by the upstream rim cavity, contoured endwall, and platform gap. Low-velocity recirculating flow was present in the upstream rim cavity. The endwall contour elevation around the suction side leading edge appeared to displace the suction side horseshoe vortex away from the airfoil-

endwall junction. The sweeping action of a vortex generated by the platform gap leakage flow resulted in a pool of oil near the throat of the passage.

The oil flow visualization patterns compared well to the measured endwall heat transfer, with the effect of the horseshoe vortex legs indicated by high heat transfer levels around the leading edge. Boundary layer disturbance due to the platform gap and leakage flow emanating from it resulted in very high heat transfer levels around the gap. Endwall film effectiveness coverage was limited by the horseshoe vortex, although leakage from the platform gap provided cooling in the throat region where heat transfer levels were high.

Increasing the platform gap leakage flowrate resulted in significantly higher heat transfer levels on the suction side platform due to increased strength of the vortical flow feature caused by the gap exit flow. Increased gap flow also resulted in more coolant present near the endwall, however, as film cooling effectiveness levels also increased around the platform gap. For the highest gap net flowrate of 0.6% MFR, platform area-averaged heat transfer increased by 8%, but effectiveness increased by 27%, relative to a gap without net leakage flow. Net heat flux to the endwall was reduced by platform gap leakage, but was not significantly reduced for gap flowrates above 0.3% MFR.

Although the effect of the non-axisymmetric contour on the endwall heat transfer or film cooling was not directly tested, previous work by the same authors (Lynch, et al. [23], Lynch, et al. [22]) suggests that the presence of the rim cavity and platform gap play a dominant role in the endwall flow pattern. The contour studied here may not significantly affect the endwall heat transfer or film cooling, compared to the effect of the leakage features. Further work in this area is necessary.

## **ACKNOWLEDGMENT**

The authors gratefully acknowledge United Technologies—Pratt & Whitney for their support of this work, particularly Atul Kohli and Christopher Lehane for their advice and technical input, and Eric Grover and Tom Praisner for performing the endwall contour design.

## **FUNDING**

Funding was provided by United Technologies—Pratt & Whitney.

Accepted Manuscript Not Copyedited

## NOMENCLATURE

$A_{gap}$	metering area of platform gap
$C$	true chord of blade
$C_{ax}$	axial chord of blade
$C_D$	discharge coefficient
$d$	diameter of film cooling hole
$h$	heat transfer coefficient, $h = q_w'' / (T_w - T_{in})$
$H$	boundary layer shape factor
$HS$	horseshoe vortex
$I$	momentum flux ratio, $I = (\rho U^2)_c / (\rho U^2)_{loc}$
$k$	thermal conductivity
$L$	length of film cooling hole, or gap overall length
$\dot{m}$	mass flow rate
$M$	blowing ratio, $M = (\rho U)_c / (\rho U)_{loc}$
MFR	mass flow ratio, $MFR = \dot{m}_c / \dot{m}_{in}$
$N$	number of film cooling holes in a group
NHFR	net heat flux reduction, see Eq. (1)
$Nu$	Nusselt number, $Nu = hC_{ax} / k_{air}$

$P$	blade pitch
$P_s$	static pressure
$PS$	pressure side
$PV$	passage vortex
$P_{tot}$	total pressure
$q''_w$	convective wall heat flux
$Re_\theta$	momentum thickness Reynolds number, $Re_\theta = \theta U_{in} / \nu$
$S$	blade span
$SS$	suction side
$T$	temperature
$x_{gap}$	distance along gap
$X, Y, Z$	global coordinates, where X is blade axial direction
$U$	average velocity magnitude
$V_{gap}$	local gap ejection/ingestion velocity
<b>Greek</b>	
$\beta$	design flow (yaw) angle
$\delta_{99}$	boundary layer thickness (99%)
$\eta$	adiabatic effectiveness, $\eta = (T_{in} - T_w) / (T_{in} - T_c)$
$\theta$	momentum thickness, or nondimensional metal temperature, $\theta = (T_{in} - T_c) / (T_{in} - T_{w,metal})$

$\nu$  kinematic viscosity

$\rho$  density

### Superscripts/Subscripts

0% case without film cooling flow

*c* leakage coolant conditions

*exit* exit freestream conditions

*in* inlet freestream conditions

*loc* local conditions

$(\bar{\quad})$  average quantity

$(\overline{\quad})$  area-averaged quantity,  $(\overline{\quad}) = \frac{\iint (\quad) \partial X \partial Y}{\iint \partial X \partial Y}$

## REFERENCES

- [1] Abo El Ella, H. M., Sjolander, S. A., and Praisner, T. J., 2012, "Effects of an Upstream Cavity on the Secondary Flow in a Transonic Turbine Cascade," *J. Turbomach.*, 134(5), pp. 051009-051009. doi: 10.1115/1.4003818.
- [2] de la Rosa Blanco, E., Hodson, H. P., and Vazquez, R., 2009, "Effect of the Leakage Flows and the Upstream Platform Geometry on the Endwall Flows of a Turbine Cascade," *J. Turbomach.*, 131(1), p. 011004.
- [3] Piggush, J., and Simon, T. W., "Flow Measurements in a First Stage Nozzle Cascade Having Leakage and Assembly Features: Effects of Endwall Steps and Leakage on Aerodynamic Losses," *Proc. ASME International Mechanical Engineering Congress and Expo, IMECE2005-83032*.
- [4] Reid, K., Denton, J. D., Pullan, G., Curtis, E., and Longley, J., "The Effect of Stator-Rotor Hub Sealing Flow on the Mainstream Aerodynamics of a Turbine," *Proc. ASME Turbo Expo 2006, GT2006-90838*.
- [5] Thrift, A. A., Thole, K. A., and Hada, S., 2012, "Effects of Orientation and Position of the Combustor-Turbine Interface on the Cooling of a Vane Endwall," *J. Turbomach.*, 134(6), pp. 061019-061019. doi: 10.1115/1.4004817.
- [6] Popović, I., and Hodson, H. P., 2013, "Aerothermal Impact of the Interaction between Hub Leakage and Mainstream Flows in Highly-Loaded High Pressure Turbine Blades," *J. Turbomach.*, 135(6), pp. 061014-061014. doi: 10.1115/1.4023621.
- [7] Popović, I., and Hodson, H. P., 2013, "Improving Turbine Stage Efficiency and Sealing Effectiveness through Modifications of the Rim Seal Geometry," *J. Turbomach.*, 135(6), pp. 061016-061016. doi: 10.1115/1.4024872.
- [8] Popović, I., and Hodson, H. P., 2013, "The Effects of a Parametric Variation of the Rim Seal Geometry on the Interaction between Hub Leakage and Mainstream Flows in High Pressure Turbines," *J. Eng. Gas Turbines Power*, 135(11), pp. 112501-112501. doi: 10.1115/1.4024867.
- [9] Reid, K., Denton, J., Pullan, G., Curtis, E., and Longley, J., 2007, "The Interaction of Turbine Inter-Platform Leakage Flow with the Mainstream Flow," *J. Turbomach.*, 129(2), pp. 303-310.
- [10] Jain, S., Roy, A., Ng, W. F., Ekkad, S., Lohaus, A. S., and Taremi, F., "Aerodynamic Performance of a Transonic Turbine Blade Passage in Presence of Upstream Slot and Mateface Gap with Endwall Contouring," *Proc. ASME IGTI Turbo Expo 2014, GT2014-26475*.
- [11] Cardwell, N. D., Sundaram, N., and Thole, K. A., 2006, "Effect of Midpassage Gap, Endwall Misalignment, and Roughness on Endwall Film-Cooling," *J. Turbomach.*, 128(1), pp. 62-70.
- [12] Piggush, J. D., and Simon, T. W., 2007, "Heat Transfer Measurements in a First-Stage Nozzle Cascade Having Endwall Contouring: Misalignment and Leakage Studies," *J. Turbomach.*, 129(4), pp. 782-790.
- [13] Lynch, S. P., and Thole, K. A., 2011, "The Effect of the Combustor-Turbine Slot and Midpassage Gap on Vane Endwall Heat Transfer," *J. Turbomach.*, 133(4), pp. 041002-041009. doi: 10.1115/1.4002950.
- [14] Roy, A., Jain, S., Ekkad, S., Ng, W. F., Lohaus, A. S., and Crawford, M. E., "Heat Transfer Performance of a Transonic Turbine Blade Passage in Presence of Leakage Flow through Upstream Slot and Mateface Gap with Endwall Contouring," *Proc. ASME IGTI Turbo Expo 2014, GT2014-26476*.

- [15] Gustafson, R., Mahmood, G. I., and Acharya, S., "Aerodynamic Measurements in a Linear Turbine Blade Passage with Three-Dimensional Endwall Contouring," *Proc. ASME Turbo Expo 2007*, GT2007-28073.
- [16] Knezevici, D. C., Sjolander, S. A., Praisner, T. J., Allen-Bradley, E., and Grover, E. A., 2010, "Measurements of Secondary Losses in a Turbine Cascade with the Implementation of Nonaxisymmetric Endwall Contouring," *J. Turbomach.*, 132(1), p. 011013. doi: 10.1115/1.3072520.
- [17] Lynch, S. P., Sundaram, N., Thole, K. A., Kohli, A., and Lehane, C., 2011, "Heat Transfer for a Turbine Blade with Nonaxisymmetric Endwall Contouring," *J. Turbomach.*, 133(1), pp. 011019-011019. doi: 10.1115/1.4000542.
- [18] Panchal, K. V., Abraham, S., Ekkad, S., Ng, W. F., Lohaus, A. S., and Crawford, M. E., "Effect of Endwall Contouring on a Transonic Turbine Blade Passage: Part 2--Heat Transfer Performance," *Proc. ASME Turbo Expo 2012*, GT2012-68405.
- [19] Schuepbach, P., Abhari, R. S., Rose, M., and Gier, J., 2011, "Influence of Rim Seal Purge Flow on Performance of an Endwall-Profiled Axial Turbine," *J. Turbomach.*, 133(2), p. 021011.
- [20] Turgut, O., and Camci, C., "Influence of Leading Edge Fillet and Nonaxisymmetric Contoured Endwall on Turbine NGV Exit Flow Structure and Interactions with Rim Seal Flow," *Proc. ASME IGTI Turbo Expo*, GT2013-95843.
- [21] Regina, K., Kalfas, A., Abhari, R. S., Lohaus, A. S., Voelker, S., and auf dem Kamp, T., "Aerodynamic Robustness of End Wall Contouring against Rim Seal Purge Flow," *Proc. ASME IGTI Turbo Expo*, GT2014-26607.
- [22] Lynch, S. P., Thole, K., Kohli, A., Lehane, C., and Praisner, T. J., 2013, "Aerodynamic Loss for a Turbine Blade with Endwall Leakage Features and Contouring," *Proc. ASME IGTI Turbo Expo 2013*, GT2013-94943.
- [23] Lynch, S. P., Thole, K., Kohli, A., Lehane, C., and Praisner, T. J., 2013, "Endwall Heat Transfer for a Turbine Blade with an Upstream Cavity and Rim Seal Leakage," *Proc. ASME IGTI Turbo Expo 2013*, GT2013-94942.
- [24] Praisner, T. J., Allen-Bradley, E., Grover, E. A., Knezevici, D. C., and Sjolander, S. A., "Application of Non-Axisymmetric Endwall Contouring to Conventional and High-Lift Turbine Airfoils," *Proc. ASME Turbo Expo 2007*, GT2007-27579.
- [25] Harvey, N. W., Rose, M. G., Taylor, M. D., Shahpar, S., Hartland, J., and Gregory-Smith, D. G., 2000, "Nonaxisymmetric Turbine End Wall Design: Part I--- Three-Dimensional Linear Design System," *J. Turbomach.*, 122(2), pp. 278-285.
- [26] MacIsaac, G. D., Sjolander, S. A., Praisner, T. J., Grover, E. A., and Jurek, R., "Effects of Simplified Platform Overlap and Cavity Geometry on the Endwall Flow: Measurements and Computations in a Low-Speed Linear Turbine Cascade," *Proc. ASME IGTI Turbo Expo*, GT2013-95670.
- [27] Kang, M. B., Kohli, A., and Thole, K. A., 1999, "Heat Transfer and Flowfield Measurements in the Leading Edge Region of a Stator Vane Endwall," *J. Turbomach.*, 121(3), pp. 558-568.
- [28] Moffat, R. J., 1988, "Describing the Uncertainties in Experimental Results," *Exp. Therm Fluid Sci.*, 1, pp. 3-17. doi: 10.1016/0894-1777(88)90043-X.
- [29] Sen, B., Schmidt, D. L., and Bogard, D. G., 1996, "Film Cooling with Compound Angle Holes: Heat Transfer," *J. Turbomach.*, 118(4), pp. 800-806.
- [30] Baldauf, S., Scheurlen, M., Schulz, A., and Wittig, S., 2002, "Heat Flux Reduction from Film Cooling and Correlation of Heat Transfer Coefficients from Thermographic Measurements

at Enginelike Conditions," *Journal of Turbomachinery-Transactions of the ASME*, 124(4), pp. 699-709. doi: 10.1115/1.1505848.

Accepted Manuscript Not Copyedited

### Figure Captions List

- Fig. 1 Depiction of the low speed wind tunnel and large scale test section
- Fig. 2 Depiction of the rim cavity, rim seal leakage geometry, and platform gap leakage geometry
- Fig. 3 Depictions of the (a) non-axisymmetric endwall contour with platform gap; (b) cross-section view of gap
- Fig. 4 Estimated platform gap leakage velocities along the gap length for the net leakage flowrates
- Fig. 5 Endwall film cooling geometry, with injection directions indicated
- Fig. 6 Comparison of (a) oil flow visualization, (b) endwall heat transfer, and (c) film cooling effectiveness for the nominal case of 0.75% MFR rim seal flow and 0.3% MFR platform gap flow
- Fig. 7 Endwall heat transfer contours for 0.75% MFR rim seal leakage with net platform gap MFR of (a) 0%, (b) 0.3%, and (c) 0.6%
- Fig. 8 Endwall heat transfer for varying platform gap MFR, extracted along an inviscid streamline path passing through the center of the passage
- Fig. 9 Heat transfer augmentation with net gap flow relative to heat transfer with 0% net gap flow, for gap MFR's of (a) 0.3% and (b) 0.6%
- Fig. 10 Film cooling effectiveness for 0.75% MFR rim seal leakage with net gap MFR of (a) 0%, (b) 0.3%, and (c) 0.6%

- Fig. 11 Endwall film cooling effectiveness for varying gap MFR, plotted along an inviscid streamline through the center of the passage
- Fig. 12 Net heat flux reduction with the addition of gap leakage flow for (a) 0.3% gap MFR, and (b) 0.6% gap MFR
- Fig. 13 Percent increase in area-averaged endwall heat transfer and film cooling, and resulting area-averaged NHFR, for increasing platform gap flow relative to 0% gap MFR

### Table Caption List

- |         |   |
|---------|---|
| Table 1 | Cascade geometry and operating conditions |
| Table 2 | Film cooling geometry and flow conditions |

Accepted Manuscript Not Copyedited

**Table 1. Cascade geometry and operating conditions**

Scale relative to engine	6X
Axial chord ( $C_{ax}$ )	0.1524 m
True chord/axial chord ( $C/C_{ax}$ )	1.36
Span/axial chord ( $S/C_{ax}$ )	3.6
Pitch/axial chord ( $P/C_{ax}$ )	1.48
Inlet angle ( $\beta_{in}$ , relative to axial direction)	31.5°
Exit angle ( $\beta_{exit}$ , relative to axial direction)	73.2°
Inlet Reynolds number ( $Re_{in}=U_{in}C_{ax}/\nu$ )	70,000
Exit Reynolds number ( $Re_{ex}=U_{exit}C_{ax}/\nu$ )	200,000
Exit Mach number	0.06
Inlet boundary layer thickness ( $\delta_{99}/S$ ), $X/C_{ax}=-1.1$	0.13
Momentum thickness ( $\theta/S$ )	0.0082
Momentum thickness Re number ( $Re_{ex}=U_{in}\theta/\nu$ )	1990
Shape factor (H)	1.32
Inlet freestream Tu, $X/C_{ax}=-5.0$	6%

**Table 2. Film cooling geometry and flow conditions**

Film cooling group	L/d	Surface angle	MFR	$M_{loc}$	$I_{loc}$
FC1 (#1-6)	11-13	22°-44°	0.1%	1.5	2.1
FC2 (#7-8)	12	40°	0.05%	1.6	2.3
FC3 (#9-12)	17-23	22°-35°	0.1%	1.6	2.3

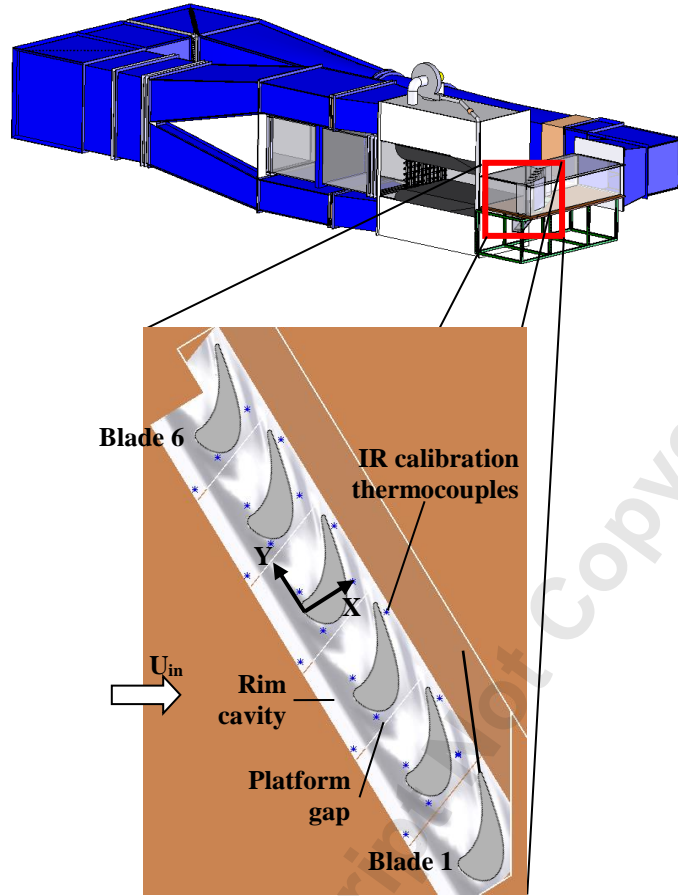


Figure 1. Depiction of the low speed wind tunnel and large scale test section.

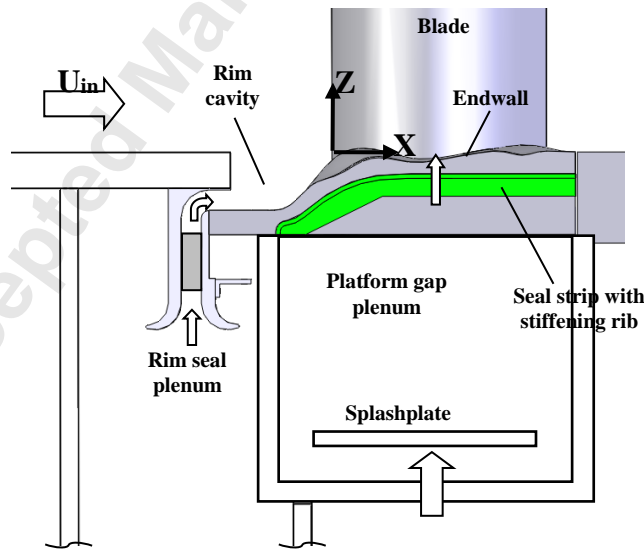


Figure 2. Depiction of the rim cavity, rim seal leakage geometry, and platform gap leakage geometry.

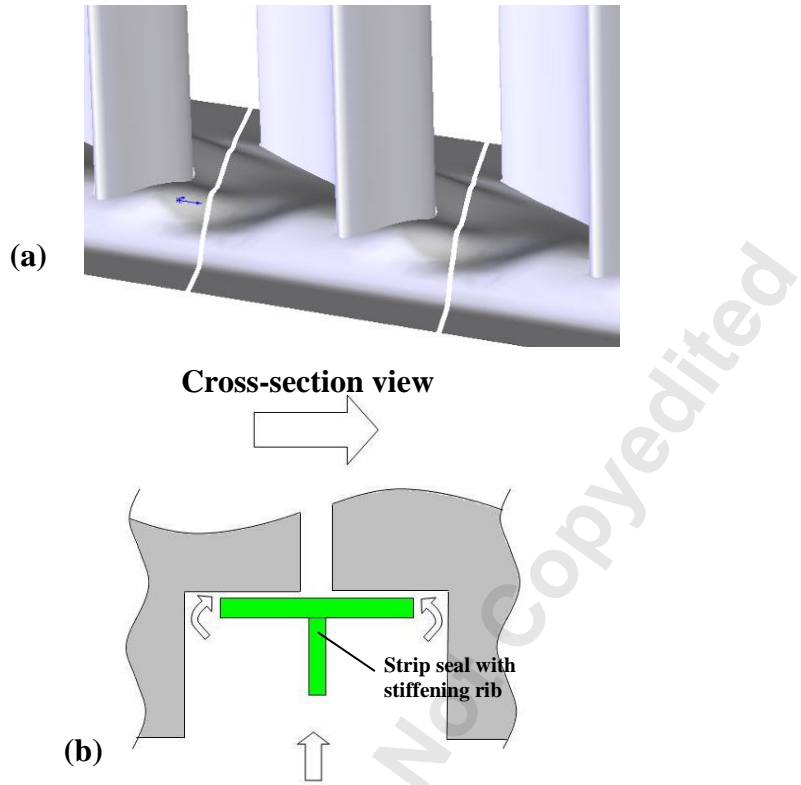


Figure 3. Depictions of the (a) non-axisymmetric endwall contour with platform gap; (b) cross-section view of gap.

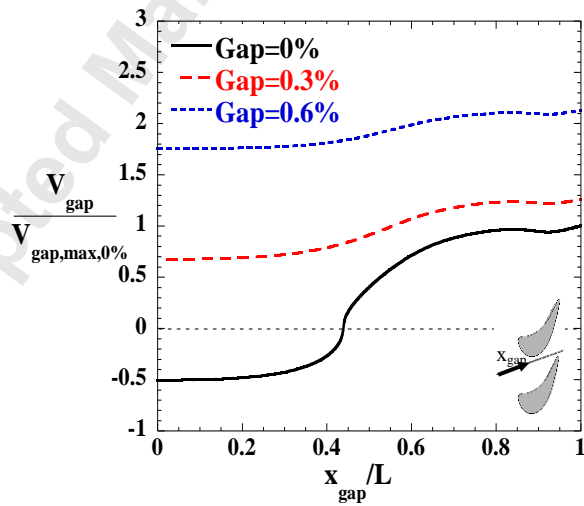


Figure 4. Estimated platform gap leakage velocities along the gap length for the net leakage flowrates.

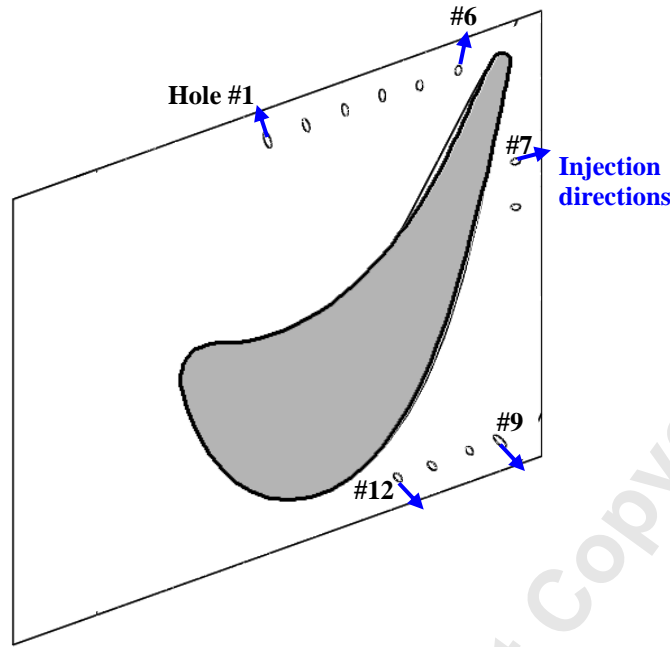


Figure 5. Endwall film cooling geometry, with injection directions indicated.

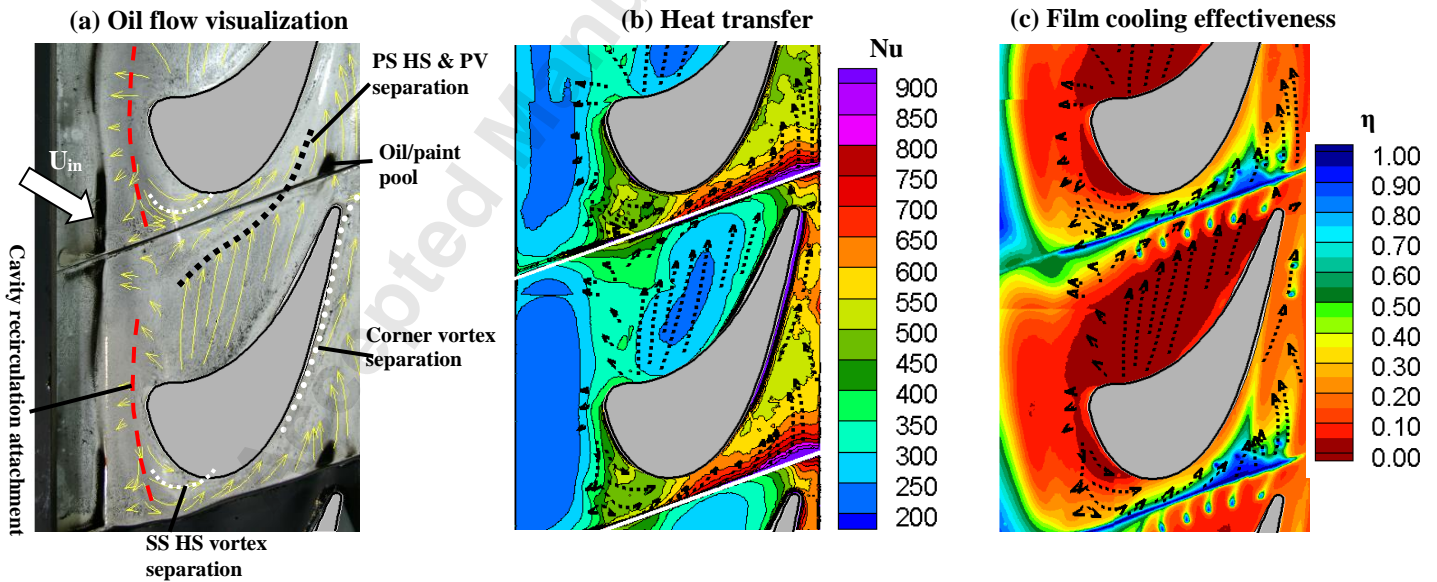


Figure 6. Comparison of (a) oil flow visualization, (b) endwall heat transfer, and (c) film cooling effectiveness for the nominal case of 0.75% MFR rim seal flow and 0.3% MFR platform gap flow.

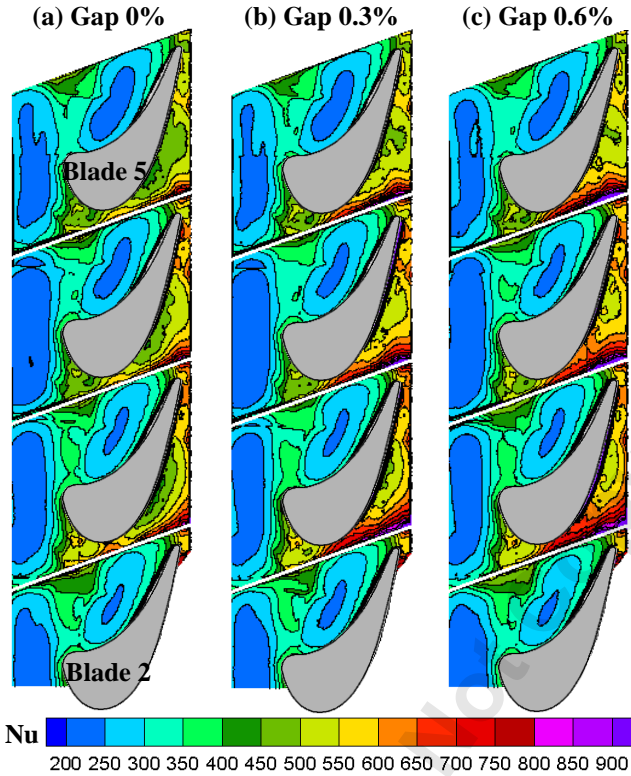


Figure 7. Endwall heat transfer contours for 0.75% MFR rim seal leakage with net platform gap MFR of (a) 0%, (b) 0.3%, and (c) 0.6%.

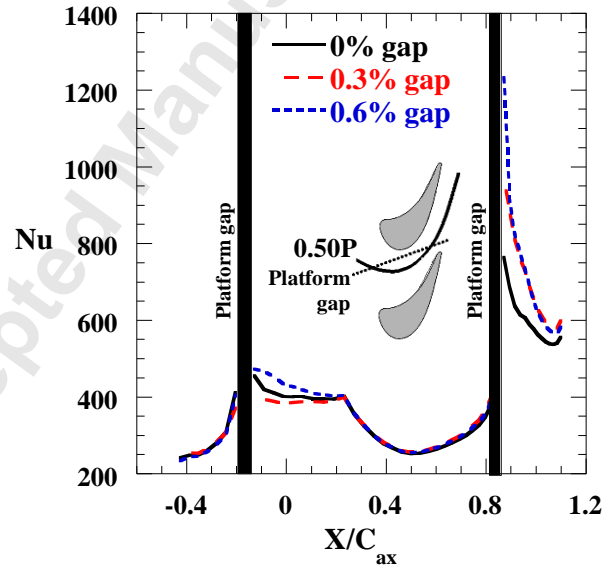


Figure 8. Endwall heat transfer for varying platform gap MFR, extracted along an inviscid streamline path passing through the center of the passage.

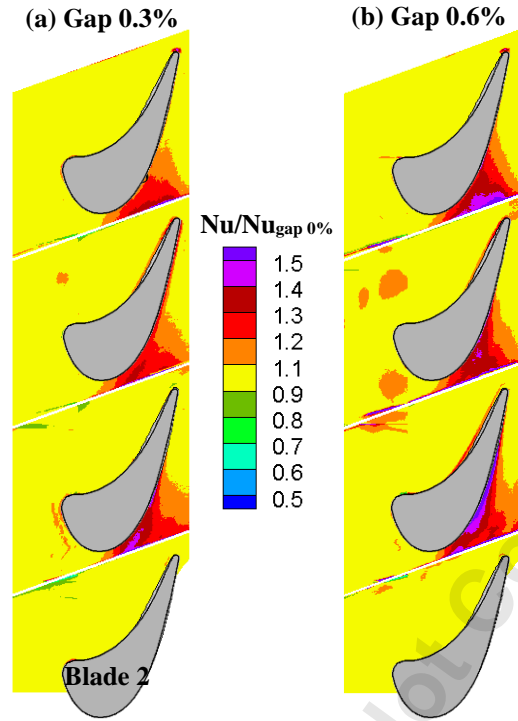


Figure 9. Heat transfer augmentation with net gap flow relative to heat transfer with 0% net gap flow, for gap MFR's of (a) 0.3% and (b) 0.6%.

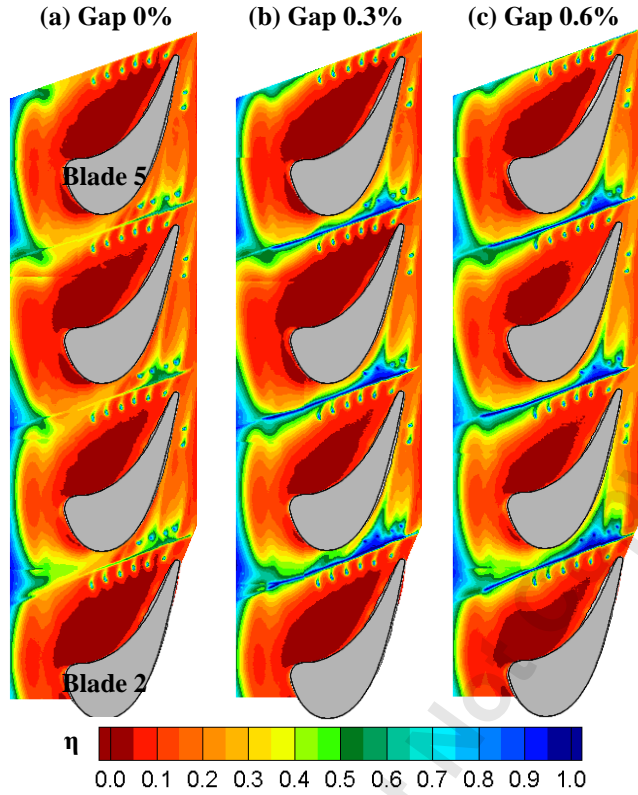


Figure 10. Film cooling effectiveness for 0.75% MFR rim seal leakage with net gap MFR of (a) 0%, (b) 0.3%, and (c) 0.6%.

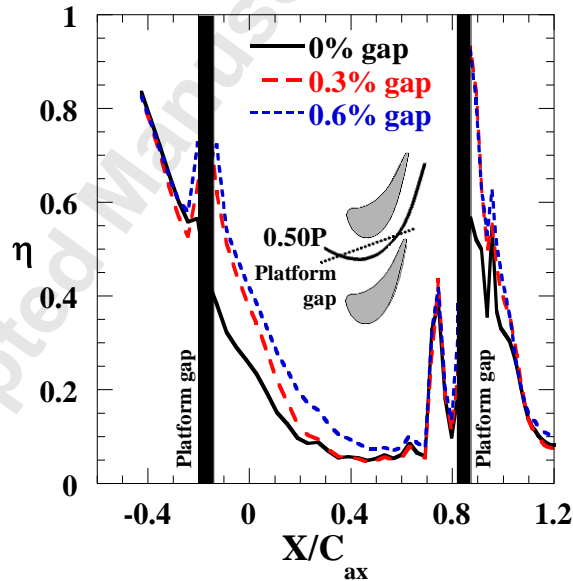


Figure 11. Endwall film cooling effectiveness for varying gap MFR, plotted along an inviscid streamline through the center of the passage.

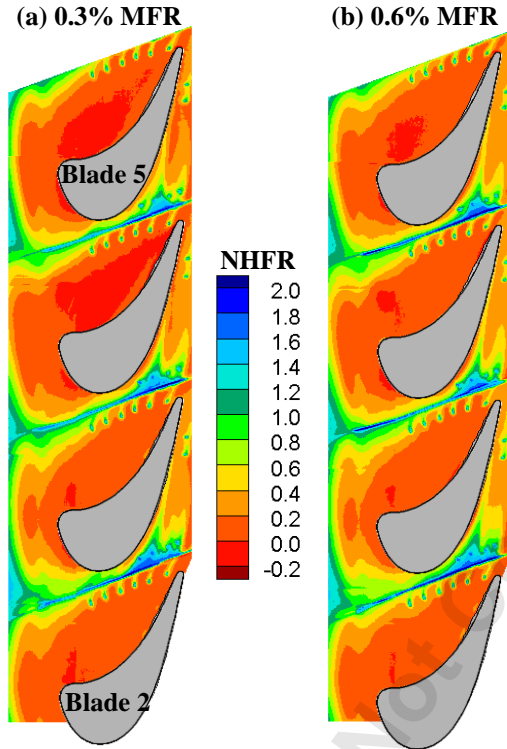


Figure 12. Net heat flux reduction with the addition of gap leakage flow for (a) 0.3% gap MFR, and (b) 0.6% gap MFR.

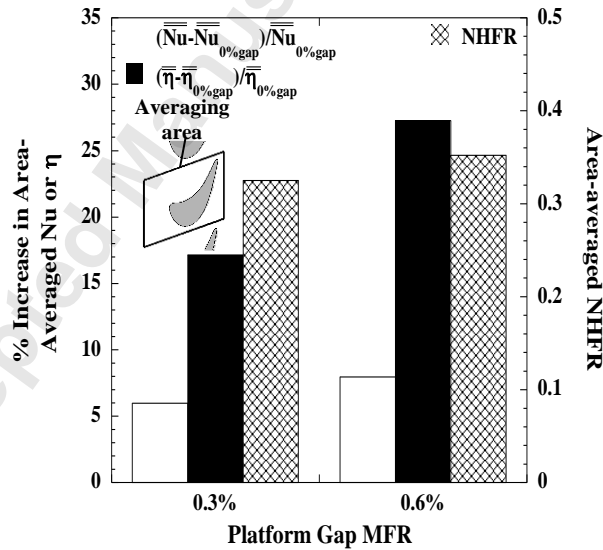


Figure 13. Percent increase in area-averaged endwall heat transfer and film cooling, and resulting area-averaged NHFR, for increasing platform gap flow relative to 0% gap MFR.